

Xenon-metal pair formation in UO_2 investigated using DFT+ U

Linu Malakkal^{1,*}, Shuxiang Zhou¹, Himani Mishra¹, Mukesh Bachhav¹,

Jia Hong Ke¹, Chao Jiang¹, Lingfeng He², and Sudipta Biswas¹

¹*Computational Mechanics and Materials Department,*

Idaho National Laboratory, Idaho Falls, ID 83415, USA and

^{1,2}*Department of Nuclear Engineering, North Carolina State University, Raleigh, NC, 27695, USA*

(Dated: February 6, 2025)

A recent experimental study on a spent uranium dioxide (UO_2) fuel sample from Belgium Reactor 3 (BR3) identified a unique pair structure formed by the noble metal phase (NMP) and fission gas (xenon [Xe]) precipitate. However, the fundamental mechanism behind this structure remains unclear. The present study aims to provide an understanding of the interaction between five different metal precipitates (molybdenum [Mo], ruthenium [Ru], palladium [Pd], technetium [Tc], and rhodium [Rh]) and the Xe fission gas atoms in UO_2 , by using density functional theory (DFT) in combination with the Hubbard U correction to compute the formation energies involved. All DFT+ U calculations were performed with occupation matrix control to ensure antiferromagnetic ordering of UO_2 . The calculated formation and binding energies of the Xe and solid fission products in the NMP reveal that these metal precipitates form stable pair structures with Xe. Notably, the formation energy of Xe-metal pairs is lower than that of the isolated single defects in all instances, with Pd and Mo showing the most favourable binding energy, likely accounting for the observed pair structure formation.

I. INTRODUCTION

Irradiation of nuclear fuels produces various fission products, which tend to segregate within different regions of the fuel's microstructure, based on their diffusivity and reactivity. Among the various fission products, a well-documented segregated phases in uranium dioxide (UO_2) [1] and mixed oxide fuels [2] are metallic precipitates primarily composed of molybdenum (Mo) and ruthenium (Ru), with smaller amounts of technetium (Tc), rhodium (Rh), and palladium (Pd). The literature refers to these metallic precipitates by various names, including white inclusion [1, 3], epsilon particles [4, 5], fission product alloys, the five metal precipitates (5MPs) (i.e., Mo, Ru, Tc, Rh, Pd) [6], and the noble metal phase (NMP) [7]. Recent studies have brought to light new insights: Buck et al. [8] reported uncertainties regarding the degree of crystallinity of these precipitates, whereas Kessler et al. [9] provided evidence for a separate non-metallic phase associated with the metallic particles. Additionally, Pellegrini et al. [10] and Kessler et al. [9] highlighted the presence of tellurium alongside the 5MPs. Given these findings, the term "NMP" is considered the most appropriate nomenclature, and we adopt this terminology so as to maintain continuity with recent scholarly work. NMP typically segregate at the grain boundaries of UO_2 [8], potentially causing fuel pellet swelling or alterations in the brittleness of surrounding materials [11], thereby impacting the mechanical properties and performance of nuclear fuel. Further, Cui et al. [12] demonstrated that these particles extracted from spent fuel components, when suspended in an aqueous solution, can catalytically

contribute to the reduction of actinides, promoting immobilization of the waste form, as is critical for effective nuclear waste management. Thus, the significance of NMP has led numerous researchers to conduct both experimental and theoretical studies to understand their formation mechanisms, size distributions, and behaviors.

The theoretical studies have primarily utilized CALPHAD [13] and *ab initio* techniques to comprehend the thermodynamics of mixing in metal alloys under varying oxygen (O) potentials. Initially, researchers reduced quinary systems to binary [7, 14–20] or ternary [21, 22] subsets in order to elucidate the thermodynamic stability of the NMP. Building on these studies, Kaye et al. [5] developed a comprehensive thermodynamic model for the quinary system. Middleburgh et al. [23] were the first to use density functional theory (DFT) to model the hexagonal structure of NMP, reporting vacancy formation energies and investigating the behavior of extrinsic defects (e.g., xenon [Xe] and iodine) in the hexagonal phase. Furthermore, King et al. [24] explored the stability, partitioning, and partial ordering of NMP systems as a function of temperature and composition. Kleykamp et al. [25, 26] investigated the composition and structure of fission product precipitates, noting that Mo is the most readily oxidized constituent of NMPs and reacts with any excess oxygen in the system. As burnup increases, oxygen is released in the oxide fuel, leading to a reduction in Mo concentration, thus making Mo content a reliable measure of burnup.

Recently, we performed advanced characterization of a spent UO_2 fuel sample with an average burnup was approximately 40 MWdkg^{-1} , from Belgium Reactor 3 (BR3) [27, 28]. Our investigation revealed that the fission product Xe forms intriguing pair structures with NMP. However, the fundamental mechanism behind these intriguing pair structures remains unknown. Although

* linu.malakkal@inl.gov

several studies have explored the stability of the NMP, the interactions between NMP and fission gases remain poorly understood. To address this knowledge gap, we employed first-principles calculations to investigate possible defect pair formations in UO_2 . Theoretical studies have previously utilized DFT simulations to understand defect energetics and diffusion of various fission products in actinide dioxides [29–38]. For example, Yun et al. [29] investigated the atomic diffusion mechanism of Xe in UO_2 through vacancy-assisted diffusion, calculating the incorporation, binding, and migration energies using DFT with spin-orbit coupling (SOC). They found that an oxygen vacancy lowers the migration energy of a uranium vacancy and suggested that the strain energy of Xe significantly contributes to the clustering of vacancies, driving the vacancy-assisted diffusion of Xe in UO_2 . Nerikar et al. [30] used DFT+ U calculations to study the stability of neutral and charged intrinsic point defects, finding that predicted equilibrium properties and defect formation energies for neutral defect complexes align well with experimental trends, though values for charged complexes were lower than measured. Thompson et al. [33] conducted DFT+ U calculations to explore the energetics of various defects in UO_2 , including noble gases (He, Ne, Ar, Kr, Xe), Schottky defects, and the interaction between these defects. Andersson et al. [32] proposed mechanisms governing fission gas evolution by analyzing Xe solution thermodynamics, migration barriers, and the interaction of dissolved Xe atoms with uranium, demonstrating that Xe diffusion predominantly occurs via a vacancy-mediated mechanism. Hong et al. [34] used DFT to investigate the solubility and clustering of Ru fission products in UO_2 suggesting that metallic dimers in Schottky defects likely form the nucleus of metallic precipitates. Cooper et al. [35] integrated DFT calculations of defect energies with empirical potential calculations of defect vibrational entropy to analyze the point defect concentrations as functions of oxygen partial pressure, temperature, and composition in $\text{UO}_{2\pm x}$. Shilpa et al. [37] recently examined the formation and migration of various neutral defects such as vacancies, interstitials, antisites, Schottky defects, and Frenkel defects in actinide oxides. Building on the work by Hong et al. [34] on the solubility and clustering of Ru fission products in UO_2 , we utilized the DFT+ U approach to understand the formation of various metal/fission-gas pair structures. We specifically characterized the formation energies, binding energy, and charge transitions of each Xe-metal pair structure, for metals of Tc, Mo, Pd, Ru, and Rh. Although it is well-established that charged defects play a crucial role in predicting specific experimental observations of UO_2 under certain irradiation conditions [30, 31, 35, 38], this study focuses exclusively on neutral defects, because the focus of this work centers on formation energies and binding energies, and it is recognized that charged defects generally lowers the predicted energy values compared to neutral defects [30]. Consequently, while restricting our analysis to neutral defects may result in slight variations in the

energy values, but will not comprise the overall conclusion of this study. For the 5MPs, our DFT+ U calculations identified the elements that are most energetically favorable to forming these pair structures. We anticipate that our results will inform future discussions regarding the impact of defect formation on the performance and stability of UO_2 . Furthermore, we expect that this work will stimulate future studies under various conditions encountered in nuclear reactors, ultimately advancing our understanding of defect dynamics in nuclear materials.

II. EXPERIMENTAL DETAILS

A focused ion beam section was extracted from the rim area of spent BR3 light-water reactor fuel with an average burnup of 4.5 at%, equivalent to approximately 40 MWd/kgU [39]. The cross-sectional sample for transmission electron microscopy was prepared using a Quanta 3D Field Emission Gun (FEG) focused ion beam system. Atomic-resolution microstructural characterization was conducted using a Titan Themis 200 transmission electron microscope (TEM) in scanning TEM (STEM) mode at Idaho National Laboratory. The spent UO_2 fuel sample was characterized via TEM at the Hot Cell Examination Facility and the Irradiated Materials Characterization Laboratory at Idaho National Laboratory [40].

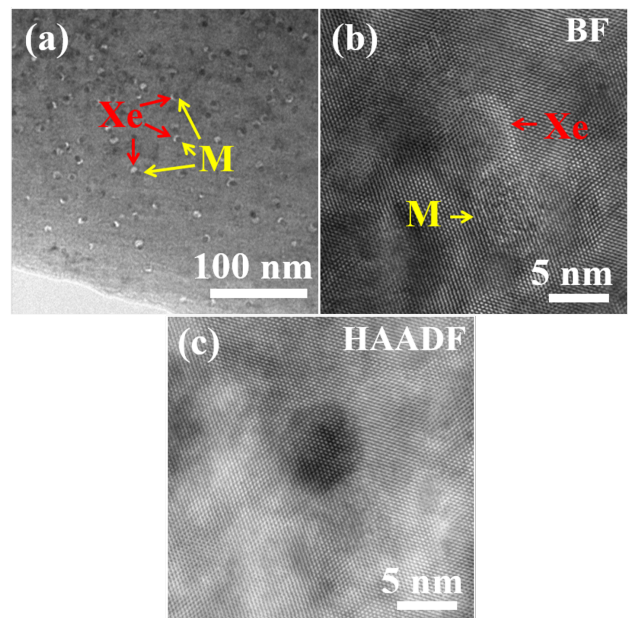


FIG. 1: (a) Bright field transmission electron microscopy (TEM) image, atomic resolution (b) Bright-field (BF) image and (c) High-angle angular dark-field (HAADF) STEM images showing the pair structure of fission gas bubbles Xe and NMP (M).

Fig. 1(a) shows the low mag TEM image of pair structure between fission Xe/Kr gas bubbles (bright features)

and NMP (M, dark features). Figs. 1(b) and (c) clearly illustrates the atomic-scale structure of a pair, with both Xe/Kr and NMP having a size of approximately 7 nm. The bright contrast observed in the bright-field image and the dark contrast in the high-angle annular dark-field image (i.e., Z-contrast) indicate a lower atomic density in the fission gas bubble as compared to the surrounding UO_2 matrix. The embedded NMP disrupts the UO_2 matrix, leading to lattice strain, which affects the contrast of the U atom columns (Figs. 1(b)). Though the crystal structure of the NMP is not fully resolved, it does not form a fully coherent interface with the UO_2 matrix.

Atom Probe Tomography (APT) analysis was conducted on UO_2 fuel to elucidate microstructural changes and the distribution of fission products. Detailed information on the APT instrument, sample preparation, and 3D reconstruction methodology is provided in the supplementary information (SI). The APT analysis site was strategically positioned adjacent to the TEM site to ensure that the same region of interest was utilized for both microstructural and chemical analysis.

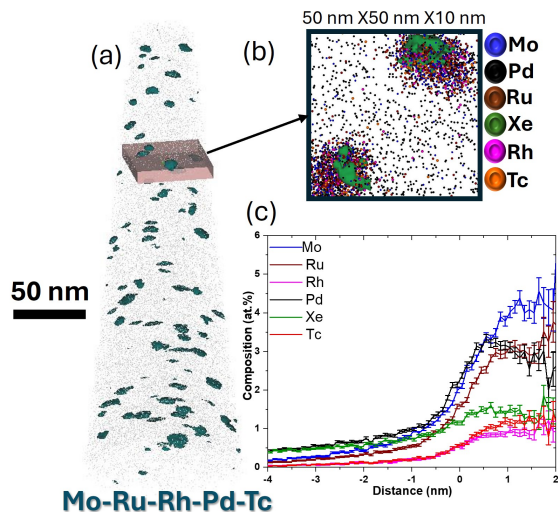


FIG. 2: (a) Representative 3D reconstruction of the UO_2 tip, (b) distribution of Mo-Tc-Ru-Rh-Pd and an iso-concentration contour of Xe in a sub-volume, (c) proxigram from precipitates taken from figure (a)

Fig. 2(a) presents a representative 3D reconstruction image of a tip, featuring an iso-concentration map that illustrates Mo-Tc-Ru-Rh-Pd precipitates uniformly distributed throughout the analyzed volume, with sizes ranging between 2-3 nm in radius. Fig. 2(b) depicts a sub-volume of a 50 nm x 50 nm x 10 nm cube, highlighting the distribution of Mo-Tc-Ru-Rh-Pd and an iso-concentration contour of Xe. Fig. 2(c) displays a proximity histogram (proxigram) plot for all precipitates, facilitating the analysis of the chemistry across all precipitates shown in Figure 2(a). It is important to note that local magnification effects in APT may impact the quantitative analysis of the size, shape, and chemistry of the five

metal precipitates and Xe, due to differences in the field evaporation behavior of the elements in the UO_2 matrix [41–43]. Nonetheless, the concentrations of Mo, Pd, and Ru are the most significant. The APT analysis reveals distinct segregation of the five metal precipitates along with Xe, corroborating the findings from TEM analysis.

III. SIMULATION DETAILS

In this work, DFT calculations were carried out using the projector augmented-wave method [44, 45], as implemented in the Vienna ab initio Simulation Package (VASP) code [46, 47]. The exchange correlation functional used was the generalized gradient approximation formulated by Perdew, Burke, and Ernzerhof [48]. To approximate the strong correlation of $5f$ electrons in UO_2 , the rotationally invariant DFT+ U approach [49] with $U = 4$ eV was employed. Spin-orbit coupling was also included in all calculations. While the ground state of UO_2 at 0 K is in a noncollinear structure of $3\mathbf{k}$ antiferromagnetic (AFM) state [50–53], it is challenging to converge all the defected structures into the $3\mathbf{k}$ AFM state, so the $1\mathbf{k}$ AFM state was applied in this work as an approximation [32, 33, 54, 55]. To converge all calculations to the designed $1\mathbf{k}$ AFM state, the occupation matrix control technique was applied. The VASP code was customized to monitor and initialize the occupation matrices during the calculation [56], and the initial values of the occupation matrices were taken from Ref. [56] (i.e., S_0 of the $1\mathbf{k}$ AFM state).

The formation energy of the Xe and five metal elements in the NMP was modeled using a $2 \times 2 \times 2$ supercell with 96 atoms for the geometrical optimizations, and the cell volume was kept constant. Although the supercell size is admittedly small, increasing the size in DFT for UO_2 is expensive due to utilization of DFT+ U and spin-orbit coupling in a noncollinear structure. It is also worth noting that the same supercell sizes were used by several researchers to tackle similar problems [34]. We implemented a $2 \times 2 \times 2$ Monkhorst–Pack k-point mesh [57], which is sufficient to avoid significant numerical error [34]. For all calculations reported herein, the cutoff energy for the plane waves was 550 eV. The convergence criteria for the energy difference was 10^{-6} eV/atom, and for the residual forces less than 10^{-3} eV/Å.

In this study, we present the formation energy as a crucial property for quantifying the ease with which the Xe-M precipitates form—specifically considering the neutral defects at substitutional uranium sites. The defect formation energy ($E_f(X)$) for a neutral defect is calculated as [58]:

$$E_f(X) = E(X) - E_0 - \sum_i n_i^X (E_i + \mu_i) \quad (1)$$

where $E(X)$ is the total energy of the defected system, E_0 is the total energy of the pristine system, n_i^X is the number of atoms of species i that were changed according

to the defect X (positive if atoms are added, negative if atoms are removed), E_i is the energy per atom in the elemental phase, and μ_i is the chemical potential of species i . To determine the energy per atom in the elemental phase, we calculated the total energy of the atom in its standard state as reference system, instead of treating it as an isolated atom. In this case, the total energy of a single atom is defined as the energy per atom in each reference system. For instance, to calculate the energy per uranium atom, we used the reference state of uranium in bulk metal (α -U). Similarly, for the energy of species such as Mo, Ru, Rh, Pd, and Tc, their elemental phases were considered Mo (bcc), Tc (hcp), Rh (fcc), Ru (hcp) and Pd (fcc). Additionally, for the energy of oxygen, we modeled oxygen molecules. Due to the well-known self-interaction error using DFT [59], an energy correction was applied using the suggested value from the fitted elemental-phase reference energies [60].

The chemical potential μ_i includes the zero-point vibrational energy and the temperature and pressure dependence of the chemical potential. By neglecting the zero-point vibration and the pressure effects, the term μ_i can be ignored. This approximation is reasonable, particularly for defect elements at zero temperature [34, 61–64]. However, it has to be noted that the oxygen chemical potential is important when considering the hyperstoichiometric UO_2 [35]. Thus, for defect elements, the third term in Equation (1) is just the DFT-calculated energy for each species. Furthermore, at equilibrium, the chemical potentials of U and O are related by the formation enthalpy of bulk UO_2 :

$$\mu_U + 2\mu_O = \Delta H_{\text{UO}_2} \quad (2)$$

where ΔH_{UO_2} is the formation enthalpy per formula unit as obtained from the DFT calculation. ΔH_{UO_2} is always negative to avoid decompose into α -U and O molecule. The values of μ_U and μ_O depend on the stoichiometry of UO_2 : in the U-rich condition, $\mu_U = 0$ and $\mu_O^{\text{min}} = \frac{1}{2}\Delta H_{\text{UO}_2}$, and in the O-rich condition, $\mu_O = 0$ and $\mu_U^{\text{min}} = \Delta H_{\text{UO}_2}$. Throughout this work, we use the O-rich condition. Finally, to understand the charge transfer between the defects, the isosurfaces of charge density were visualized using the VESTA package [65].

IV. RESULTS AND DISCUSSION

In this study, we examined five different types of defect pairs in UO_2 , denoted as Xe-M (where M represents Mo, Ru, Rh, Tc, and Pd). To calculate the formation energy, we conducted structural optimization on UO_2 by substituting the U sites with one metal atom, one Xe atom, two metal atoms, two Xe atoms, and one metal atom combined with one Xe atom. We limited our investigation to the substitution of defects in the U vacancy, as it is the most energetically favorable trap site for several fission products [30, 34, 66], due to the significant mismatch in atomic sizes between O and Xe, and between O

and M. The relaxed structure of the Xe-Mo defect pair, used to calculate its formation energy, is presented in Fig. 3. Upon analyzing the relaxed structure, we observe that apart from the distorted nearest O atoms, when two Xe atoms are substituted in nearby U sites, one of them moves away from its original position, as shown in Fig 3(d), (a U atom was removed from Figure 3(d) to show the moved Xe atom). For the sake of brevity in this article, the relaxed structures of all other Xe-M pairs are provided in the supplementary information (SI-Fig 1).

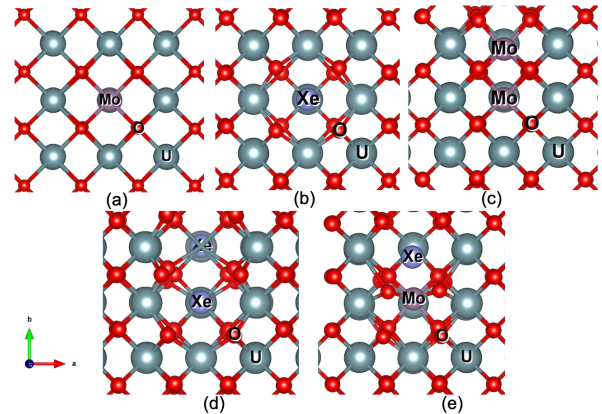


FIG. 3: Relaxed structure of the Xe-Mo pair in UO_2 fuel with atoms having been substituted in the U site (a) Mo, (b) Xe, (c) two Mo atoms, (d) two Xe atoms, and (e) one Xe atom combined with one Mo atom.

To gain a deeper understanding of the observed defect pair structure, we conducted a comprehensive analysis of the charge density profiles for all Xe-M pairs. The charge density difference for the Xe-Mo pair is illustrated in Fig. 3, and the remaining cases are provided in the SI-Fig 2. In the isosurface regions, yellow denotes charge accumulation, while blue signifies charge depletion. The isosurface level was kept constant at a value of $4.64 \times 10^{-2} e\text{Bohr}^{-3}$ for the overall charge density analysis. Our findings reveal significant charge depletion around Mo dopant sites, a trend consistent across other dopants (Xe and various metals). Additionally, when a single metal atom substitutes at a uranium site, there is a symmetrical accumulation of charge on the nearest oxygen atoms for most metals, except for Rh and Pd. This exception can be attributed to the highly filled valence orbitals in Rh and Pd. However, in the presence of Xe, charge accumulation extends to the next-nearest neighbors, likely due to the dangling bonds at these locations. The most significant charge redistribution is observed in cases where both Xe and metal atoms are present. These findings necessitate further investigation of the Bader charges on the dopant atoms and the host lattice.

The Bader charges on various atoms for all possible defect configurations are listed in SI Table 1, where (q) denotes the Bader charge present on each atom. We observe a consistent pattern in the Bader charges for U and

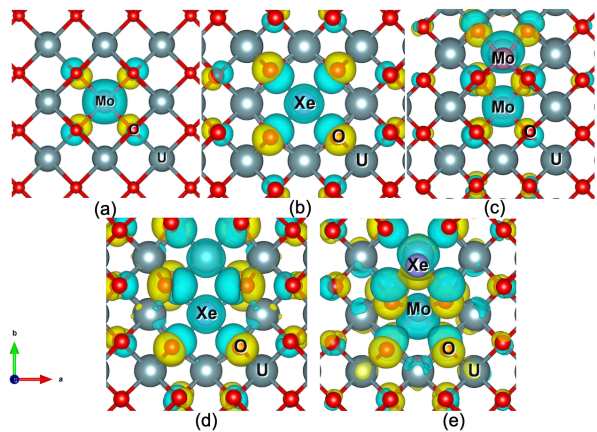


FIG. 4: Charge density difference plot of the Xe-Mo pair in UO_2 fuel with atoms having been substituted in the U site (a) Mo, (b) Xe, (c) two Mo atoms, (d) two Xe atoms, and (e) one Xe combined with one Mo atom.

O, with U exhibiting values around 11.31 to 11.41 and O around 7.26 to 7.30, across different defect configurations. However, an intriguing trend is observed when examining the Bader charges for Xe and various metal atoms. The analysis reveals that the Bader charge on the Xe atom is relatively higher, indicating that Xe, as a noble gas, retains a significant amount of its electronic charge. Whereas, metal atoms show varying degrees of electron transfer, with Mo showing the most significant charge reduction and Pd retaining the highest charge. Specifically in the case of M-Xe- UO_2 configurations, the Mo-Xe- UO_2 system exhibits the lowest metal charge, signifying a strong electron transfer from Mo. This significant charge depletion in Mo results in notable charge delocalization, which is corroborated by the charge difference density results, as illustrated in Fig. 3. This charge delocalization likely plays a critical role in stabilizing the structure. These findings provide crucial insights into the electronic interactions and charge distributions in M-Xe pair formation, highlighting the unique behaviour of Mo.

To understand the formation energy of Xe-metal pairs, we first calculated the formation energy of single defects. The single defects in UO_2 were constructed by replacing one U atom with either a Xe, Mo, Ru, Rh, Pd, or Tc atom. The relaxed-structure schematics for the single-atom Xe and Mo substitutions are shown in Fig. 3 (a), with all other single-defect relaxed structures being provided in the SI. The formation energy in an O-rich environment, as calculated using Equation 1 for all single defects considered in this work, is shown in Fig. 4. Among all the single defects analyzed, the Mo atom exhibits the lowest formation energy, indicating that the smallest energy penalty is incurred when substituting Mo at a U site. This is followed by Tc, Ru, Rh, Pd, and Xe. It is notable that the formation energy for single Mo and Tc atoms in UO_2 is negative, indicating a solution in the lat-

tice. However, given the experimental evidence of NMP formation, it is reasonable to deduce that the presence of other metals makes the formation of a separate phase thermodynamically more favorable. This suggests a complex interaction that warrants further computational investigation using larger length scale modeling. Following the analysis of single defects, we calculated the formation energies of dimer defects of the same species, with two atoms of Xe, Mo, Ru, Rh, Pd, or Tc being substituted at two neighboring U sites. The calculated formation energies of the dimers are listed in Fig. 4 (b) (denoted as “coupled”), in comparison with the formation energies measured when the two defects are spaced infinitely far apart (“isolated”). The total formation energy of the two isolated defects was estimated by summing together the formation energies of each individual defect.

Figure 4 (b) clearly demonstrates that coupled dimers are energetically more favorable than dispersed atoms. Specifically, the $\text{Xe}_U\text{-Xe}_U$, $\text{Ru}_U\text{-Ru}_U$, $\text{Pd}_U\text{-Pd}_U$, and $\text{Ta}_U\text{-Ta}_U$ pairs show a reduction in formation energy when in close proximity. In contrast, the changes in formation energy for $\text{Rh}_U\text{-Rh}_U$ and $\text{Mo}_U\text{-Mo}_U$ are marginal. These results indicate that metal atoms tend to form metallic clusters in UO_2 fuel, rather than existing as dispersed atoms. Finally, we computed the formation energies of defect pairs involving Xe and various metals (Mo, Ru, Rh, Tc, and Pd) and compared these with the formation energies pertaining to when the metal and Xe atoms are isolated, as illustrated in Fig. 4 (c). Our results demonstrate that the formation energies of Xe-metal pairs are consistently lower than those of isolated defects, suggesting Xe-metal pair defects to be energetically favorable. Among the metals studied, the Xe-Mo pair exhibited the lowest formation energy, followed sequentially by Tc, Ru, Pd, and Rh. Furthermore, we calculated the binding energy of Xe-metal pairs, as illustrated in Fig. 4 (d). The results suggest that Xe-metal interactions are energetically favorable, with the highest binding energy observed for the Xe-Pd pair, followed by the Xe-Mo pair. Charge transfer analysis indicated that the charge transfer between Pd and Xe is negligible. Consequently, we attribute the substantial binding energy in the Xe-Pd system primarily to minimal mismatch between the strain field, as Pd as the closest atomic radii as that of Xe, among the five metal precipitates studied. This could potentially reduce the overall energy of the system, leading to a higher binding energy. In the case of the Xe-Mo pair, the binding energy arises from a combination of local charge redistribution and the change of strain field. In summary, the strong binding energies for the Xe-metal pairs can be attributed to a synergistic effect of charge transfer and change of strain field upon the formation of the Xe-metal pairs. This finding indicates that, of the metals investigated in this study, Pd and Mo are the most likely candidates to form stable pair structures with Xe.

Note that while the Xe-M pair formation energies can serve as an important milestone for studying the for-

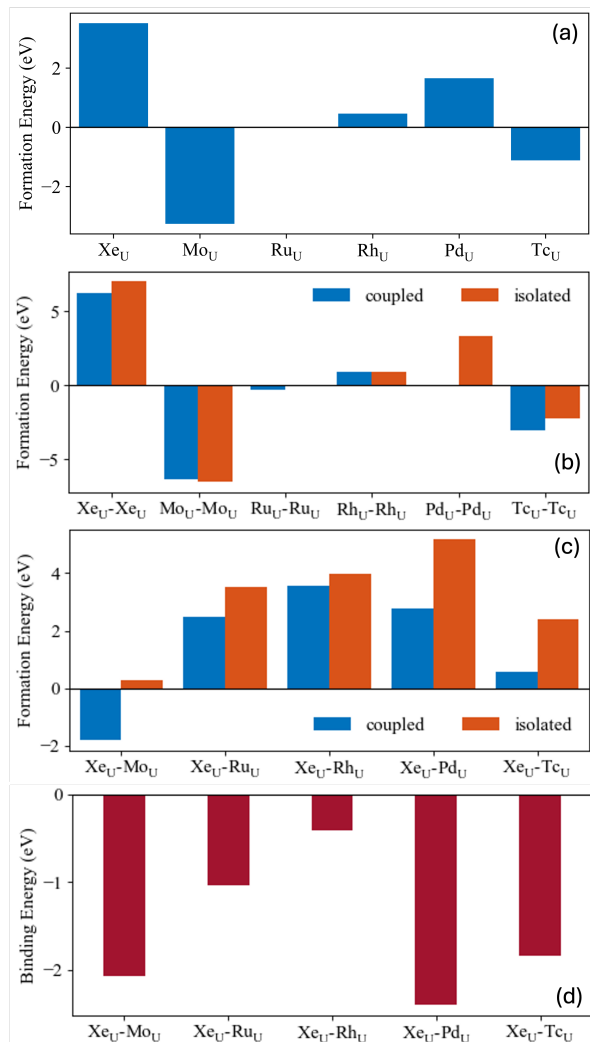


FIG. 5: (a) Calculated formation energies of single defects at the U site, in the following order: Xe, Mo, Ru, Rh, Pd, and Tc. (b) Pair formation energies of dimers of the same species (blue), as compared to when these defects are isolated (orange). (c) Pair formation energies of dimers of the Xe-metal (blue), as compared to when these defects are isolated (orange). (d) Binding energy calculated by taking the energy difference for separated and coupled Xe-metal pairs

mation of clusters and precipitates, a multiscale modeling approach will be necessary to investigate the stability and morphology of the pair cluster formation as observed in Fig. 1(b). Simulation of the Xe-M clusters requires a robust description of the interatomic energies (e.g., binding or formation energies of clusters as a function of size and solute type) with *ab initio* accuracy for a wide variety of cluster configurations. Specifically, a combination of DFT, mean-field, and coarse-grained approaches that involve cluster dynamics and statistical sampling [67] will be important for capturing Xe-M cluster evolutions. These evolutions can be captured by

determining the rate processes of multiple cluster reactions (e.g., absorption, desorption, and re-solution) and diffusion events, and these rate processes will be used to parameterize multiscale models. The cluster dynamics model and statistical sampling have seen successful applications for investigating the stability and evolution of precipitates [68] and solute/defect clusters [69–71] in structural alloys. The integrated multiscale approach is currently beyond the scope of this study; future research will aim to incorporate this approach for a more comprehensive understanding.

V. CONCLUSION

In conclusion, we employed DFT+*U* calculations to unravel the fundamental mechanism underlying the formation of Xe-M pair structures in spent UO₂ fuel samples from BR3. Our study calculated the formation energies and binding energies of five Xe-metal pairs, both in close proximity and in isolation. The results revealed that the formation energies of Xe-metal pairs are consistently lower than those of single defects, indicating enhanced stability for paired configurations. The binding energy of the Xe-M pairs follows the order of Xe-Pd > Xe-Mo > Xe-Tc > Xe-Ru > Xe-Rh, clearly highlighting that Pd and Mo are the most favorable metal for forming stable structures with Xe among the five metals considered. We attribute the stability of the metal-Xe pair to a synergistic effect of charge transfer and the change of strain field upon the formation of the Xe-metal pairs. Also, the APT analysis suggests that the concentration of Mo, Pd and Ru is relatively higher in the NMPs, indicating that these elements likely govern the fundamental mechanisms. This elucidation of the pair formation mechanism significantly advances our understanding of fission product behavior in nuclear fuels. Future energy-dispersive X-ray spectroscopy analyses of the BR3 samples are planned to further substantiate these findings through experimental validation. These insights enhance our comprehension of defect interactions in nuclear fuel matrices.

VI. ACKNOWLEDGMENTS

This work was supported through Idaho National Laboratory (INL)'s Laboratory Directed Research and Development (LDRD) Program under U.S. Department of Energy (DOE)-Idaho Operations Office Contract DE-AC07-05ID14517. The authors also acknowledge that this research made use of the resources of the High Performance Computing Center at INL, which is supported by the DOE Office of Nuclear Energy and the Nuclear Science User Facilities under contract no. DE-AC07-05ID14517. The U.S. Government retains and the publisher, by accepting the article for publication, acknowledges that the U.S. Government retains a nonexclusive, paid-up, irre-

vocable, world-wide license to publish or reproduce the

published form of this manuscript, or allow others to do so, for U.S. Government purposes.

-
- [1] B. Bradbury, J. Demant, P. Martin, and D. Poole, Electron probe micro-analysis of irradiated UO_2 , *Journal of Nuclear Materials* **17**, 227 (1965).
- [2] D. O'boyle, F. Brown, and A. Dwtght, Analysis of fission product ingots formed in uranium-plutonium oxide irradiated in EBR-II, *Journal of Nuclear Materials* **35**, 257 (1970).
- [3] J. Bramman, R. Sharpe, D. Thom, and G. Yates, Metallic fission-product inclusions in irradiated oxide fuels, *Journal of Nuclear Materials* **25**, 201 (1968).
- [4] S. Imoto, Chemical state of fission products in irradiated UO_2 , *Journal of Nuclear Materials* **140**, 19 (1986).
- [5] M. Kaye, B. Lewis, and W. Thompson, Thermodynamic treatment of noble metal fission products in nuclear fuel, *Journal of Nuclear Materials* **366**, 8 (2007).
- [6] R. Scheele, B. McNamara, A. M. Casella, and A. Kozelisky, On the use of thermal NF_3 as the fluorination and oxidation agent in treatment of used nuclear fuels, *Journal of Nuclear Materials* **424**, 224 (2012).
- [7] H. Kleykamp, The chemical state of the fission products in oxide fuels, *Journal of Nuclear Materials* **131**, 221 (1985).
- [8] E. C. Buck, E. J. Mausolf, B. K. McNamara, C. Z. Soderquist, and J. M. Schwantes, Nanostructure of metallic particles in light water reactor used nuclear fuel, *Journal of Nuclear Materials* **461**, 236 (2015).
- [9] S. H. Kessler, T. G. Lach, K. E. Garrett, M. A. Conroy, D. G. Abrecht, J. M. Schwantes, and R. A. Clark, Direct observations of Pd-Te compound formation within noble metal inclusions in spent nuclear fuel, *Journal of Nuclear Materials* **538**, 152249 (2020).
- [10] K. L. Pellegrini, C. Z. Soderquist, S. D. Shen, E. J. Krogstad, C. J. Palmer, K. R. Gerez, E. C. Buck, T. G. Lach, J. M. Schwantes, and R. A. Clark, Chemical and isotopic characterization of noble metal phase from commercial UO_2 fuel, *Analytical Chemistry* **91**, 10.1021/acs.analchem.8b05549 (2019).
- [11] I. Ray, H. Thiele, and H. Matzke, Transmission electron microscopy study of fission product behaviour in high burnup UO_2 , in *Nuclear Materials for Fission Reactors*, European Materials Research Society Symposia Proceedings, edited by H. Matzke and G. Schumacher (Elsevier, Oxford, 1992) pp. 90–95.
- [12] D. Cui, J. Low, V. Rondinella, and K. Spahiu, Hydrogen catalytic effects of nanostructured alloy particles in spent fuel on radionuclide immobilization, *Applied Catalysis B: Environmental* **94**, 173 (2010).
- [13] N. Saunders and A. Miodownik, *CALPHAD (calculation of Phase Diagrams): A Comprehensive Guide*, Pergamon materials series (Elsevier Science & Technology Books, 1998).
- [14] G. Chattopadhyay, Y. Bhatt, and S. Khera, Phase diagram of the Pd-Te system, *Journal of the Less Common Metals* **123**, 251 (1986).
- [15] H. Kleykamp, Constitution and thermodynamics of the Mo-Ru, Mo-Pd, Ru-Pd and Mo-Ru-Pd systems, *Journal of Nuclear Materials* **167**, 49 (1989).
- [16] M. Kelm, A. Görtzen, H. Kleykamp, and H. Penttinghaus, On the constitution of the Pd-Te system up to 28 at.% Te, *Journal of the Less Common Metals* **166**, 125 (1990).
- [17] T. Matsui and K. Naito, Vaporization study on fission-produced noble metal alloys by mass-spectrometric method, *Thermochemica Acta* **139**, 299 (1989).
- [18] T. Matsui, T. Hoshikawa, and K. Naito, Oxidation of simulated fission-produced noble metals and alloy, *Solid State Ionics* **40-41**, 996 (1990).
- [19] A. E. Kissavos, S. Shallcross, M. V., K. L., and I. A. Abrikosov, A critical test of ab initio and CALPHAD methods: The structural energy difference between bcc and hcp molybdenum, *Calphad* **29**, 17 (2005).
- [20] A. E. Kissavos, S. Shallcross, L. Kaufman, O. Grånäs, A. V. Ruban, and I. A. Abrikosov, Thermodynamics of ordered and disordered phases in the binary Mo-Ru system, *Phys. Rev. B* **75**, 184203 (2007).
- [21] A. Dwight and D. O'Boyle, Phase studies on fission product alloys, *Journal of Nuclear Materials* **136**, 280 (1985).
- [22] L. Cornish and J. Pratt, Constitutional studies of the molybdenum-ruthenium-palladium ternary system, *Journal of Alloys and Compounds* **247**, 66 (1997).
- [23] S.C.Middleburgh, D. M. King, and G. Lumpkin, Atomic scale modelling of hexagonal structured metallic fission product alloys, *Royal Society* **2** (2015).
- [24] D. King, P. Burr, E. Obbard, and S. Middleburgh, DFT study of the hexagonal high-entropy alloy fission product system, *Journal of Nuclear Materials* **488**, 70 (2017).
- [25] H. Kleykamp, J. Paschoal, R. Pejsa, and F. Thümmeler, Composition and structure of fission product precipitates in irradiated oxide fuels: Correlation with phase studies in the Mo-Ru-Rh-Pd and BaO- UO_2 - ZrO_2 - MoO_2 systems, *Journal of Nuclear Materials* **130**, 426 (1985).
- [26] H. Kleykamp, The chemical state of the fission products in oxide fuels, *Journal of Nuclear Materials* **131**, 221 (1985).
- [27] A. S. Ditter, D. E. Smiles, D. Lussier, A. B. Altman, M. Bachhav, L. He, M. W. Mara, C. Degueldre, S. G. Minasian, and D. K. Shuh, Chemical and elemental mapping of spent nuclear fuel sections by soft X-ray spectromicroscopy, *Journal of Synchrotron Radiation* **29**, 67 (2022).
- [28] R. Yuan, J. Zhang, L. He, and J.-M. Zuo, Training artificial neural networks for precision orientation and strain mapping using 4D electron diffraction datasets, *Ultramicroscopy* **231**, 113256 (2021).
- [29] Y. Yun, H. Kim, H. Kim, and K. Park, Atomic diffusion mechanism of Xe in UO_2 , *Journal of Nuclear Materials* **378**, 40 (2008).
- [30] P. Nerikar, T. Watanabe, J. S. Tulenko, S. R. Phillpot, and S. B. Sinnott, Energetics of intrinsic point defects in uranium dioxide from electronic-structure calculations, *Journal of Nuclear Materials* **384**, 61 (2009).
- [31] J.-P. Crocombette, D. Torumba, and A. Chartier, Charge states of point defects in uranium oxide calculated with a local hybrid functional for correlated electrons, *Phys. Rev. B* **83**, 184107 (2011).

- [32] D. A. Andersson, B. P. Uberuaga, P. V. Nerikar, C. Unal, and C. R. Stanek, U and Xe transport in $\text{UO}_{2\pm x}$: Density functional theory calculations, *Phys. Rev. B* **84**, 054105 (2011).
- [33] A. E. Thompson and C. Wolverton, First-principles study of noble gas impurities and defects in UO_2 , *Phys. Rev. B* **84**, 134111 (2011).
- [34] M. Hong, S. R. Phillpot, C.-W. Lee, P. Nerikar, B. P. Uberuaga, C. R. Stanek, and S. B. Sinnott, Solubility and clustering of ruthenium fission products in uranium dioxide as determined by density functional theory, *Phys. Rev. B* **85**, 144110 (2012).
- [35] M. Cooper, S. Murphy, and D. Andersson, The defect chemistry of $\text{UO}_{2\pm x}$ from atomistic simulations, *Journal of Nuclear Materials* **504**, 251 (2018).
- [36] J. Rest, M. Cooper, J. Spino, J. Turnbull, P. Van Uffelen, and C. Walker, Fission gas release from UO_2 nuclear fuel: A review, *Journal of Nuclear Materials* **513**, 310 (2019).
- [37] S. Singh, Y. Sonvane, K. Nekrasov, A. Kupryazhkin, P. Gajjar, and S. K. Gupta, A first principles investigation of defect energetics and diffusion in actinide dioxides, *Journal of Nuclear Materials* **591**, 154901 (2024).
- [38] W. D. Neilson, J. Rizk, M. W. D. Cooper, and D. A. Andersson, Oxygen potential, uranium diffusion, and defect chemistry in $\text{UO}_{2\pm x}$: A density functional theory study, *Journal of Physical Chemistry C* **128**, 21559 – 21571 (2024), cited by: 0.
- [39] S. Herrmann, L. Shelly, and M. Simpson, Electrolytic reduction of spent light water reactor fuel bench-scale experiment results, *Journal of Nuclear Science and Technology* **44**, 361 (2007).
- [40] S. Sakib, Y. Lu, C. B. Howard, C. Jiang, S. Biswas, D. Yushu, J. Burns, W.-Y. Chen, and L. He, In-situ ion irradiation of a spent UO_2 fuel, in *Proceedings of the ANS* (American Nuclear Society, Las Vegas Nevada, 2024) pp. 642–643.
- [41] F. Vurpillot, A. Bostel, and D. Blavette, Trajectory overlaps and local magnification in three-dimensional atom probe, *Applied Physics Letters* **76**, 3127 (2000).
- [42] E. A. Marquis and F. Vurpillot, Chromatic aberrations in the field evaporation behavior of small precipitates, *Microscopy and Microanalysis* **14**, 561 (2008).
- [43] F. De Geuser, W. Lefebvre, F. Danoix, F. Vurpillot, B. Forbord, and D. Blavette, An improved reconstruction procedure for the correction of local magnification effects in three-dimensional atom-probe, *Surface and Interface Analysis* **39**, 268 (2007).
- [44] P. E. Blöchl, Projector augmented-wave method, *Physical Review B* **50**, 17953 (1994).
- [45] G. Kresse and D. Joubert, From ultrasoft pseudopotentials to the projector augmented-wave method, *Physical Review B* **59**, 1758 (1999).
- [46] G. Kresse and J. Hafner, Ab initio molecular dynamics for liquid metals, *Physical Review B* **47**, 558 (1993).
- [47] G. Kresse and J. Furthmüller, Efficient iterative schemes for ab initio total-energy calculations using a plane-wave basis set, *Physical Review B* **54**, 11169 (1996).
- [48] J. P. Perdew, K. Burke, and M. Ernzerhof, Generalized Gradient Approximation Made Simple, *Physical Review Letters* **77**, 3865 (1996).
- [49] S. L. Dudarev, G. A. Botton, S. Y. Savrasov, C. J. Humphreys, and A. P. Sutton, Electron-energy-loss spectra and the structural stability of nickel oxide: An LSDA+U study, *Physical Review B* **57**, 1505 (1998).
- [50] P. Burel, J. Rossat-Mignod, S. vuevel, O. Vogt, J. C. Spirlet, and J. Rebigant, Neutron diffraction on actinides, *Journal of the Less Common Metals Proceedings of Actinides 85, Aix en Provence - Part I*, **121**, 121 (1986).
- [51] K. Ikushima, S. Tsutsui, Y. Haga, H. Yasuoka, R. E. Walstedt, N. M. Masaki, A. Nakamura, S. Nasu, and Y. Ōnuki, First-order phase transition in UO_2 : ^{235}U and ^{17}O NMR study, *Physical Review B* **63**, 104404 (2001).
- [52] E. Blackburn, R. Caciuffo, N. Magnani, P. Santini, P. J. Brown, M. Enderle, and G. H. Lander, Spherical neutron spin polarimetry of anisotropic magnetic fluctuations in UO_2 , *Physical Review B* **72**, 184411 (2005).
- [53] S. Wilkins, R. Caciuffo, C. Detlefs, J. Rebizant, E. Colineau, F. Wastin, and G. H. Lander, Direct observation of electric-quadrupolar order in UO_2 , *Physical Review B* **73**, 060406 (2006).
- [54] J.-P. Crocombette, Influence of charge states on energies of point defects and clusters in uranium dioxide, *Physical Review B—Condensed Matter and Materials Physics* **85**, 144101 (2012).
- [55] B. Dorado, M. Freyss, B. Amadon, M. Bertolus, G. Jomard, and P. Garcia, Advances in first-principles modelling of point defects in UO_2 : f electron correlations and the issue of local energy minima, *Journal of Physics: Condensed Matter* **25**, 333201 (2013).
- [56] S. Zhou, H. Ma, E. Xiao, K. Gofryk, C. Jiang, M. E. Manley, D. H. Hurley, and C. A. Marianetti, Capturing the ground state of uranium dioxide from first principles: Crystal distortion, magnetic structure, and phonons, *Physical Review B* **106**, 125134 (2022).
- [57] H. J. Monkhorst and J. D. Pack, Special points for brillouin-zone integrations, *Phys. Rev. B* **13**, 5188 (1976).
- [58] E. Sezen, S. M. Oner, C. Deger, and I. Yavuz, Defect pair formation in FAPbI_3 perovskite solar cell absorbers, *The Journal of Physical Chemistry Letters* **13**, 9718 (2022).
- [59] A. Droghetti, C. D. Pemmaraju, and S. Sanvito, Predicting d^0 magnetism: Self-interaction correction scheme, *Physical Review B* **78**, 140404 (2008).
- [60] V. Stevanović, S. Lany, X. Zhang, and A. Zunger, Correcting density functional theory for accurate predictions of compound enthalpies of formation: Fitted elemental-phase reference energies, *Physical Review B* **85**, 115104 (2012).
- [61] J. P. Crocombette, F. Jollet, L. T. Nga, and T. Petit, Plane-wave pseudopotential study of point defects in uranium dioxide, *Phys. Rev. B* **64**, 104107 (2001).
- [62] H. Zhu, C. Tang, and R. Ramprasad, Phase equilibria at HfO_2 and Pt-HfO_2 interfaces from first principles thermodynamics, *Phys. Rev. B* **82**, 235413 (2010).
- [63] K. Reuter and M. Scheffler, Composition, structure, and stability of RuO_2 as a function of oxygen pressure, *Phys. Rev. B* **65**, 035406 (2001).
- [64] S. Zhou, Z. Hua, K. K. Bawane, H. Zhou, and T. Feng, Impacts of point defects on shallow doping in cubic boron arsenide: A first principles study, *Computational Materials Science* **247**, 113483 (2025).
- [65] K. Momma and F. Izumi, *VESTA3* for three-dimensional visualization of crystal, volumetric and morphology data, *Journal of Applied Crystallography* **44**, 1272 (2011).
- [66] G. Brillant, F. Gupta, and A. Pasturel, Fission products stability in uranium dioxide, *Journal of Nuclear Materials* **412**, 170 (2011).
- [67] J.-H. Ke, Microstructure modeling of nuclear structural materials: Recent progress and future directions, *Com-*

- putational Materials Science **230**, 112503 (2023).
- [68] J. Lepinoux, Modelling precipitation in binary alloys by cluster dynamics, *Acta Materialia* **57**, 1086 (2009).
- [69] J.-H. Ke and B. W. Spencer, Cluster dynamics modeling of Mn-Ni-Si precipitates coupled with radiation-induced segregation in low-Cu reactor pressure vessel steels, *Journal of Nuclear Materials* **569**, 153910 (2022).
- [70] M. Jin, C. Permann, and M. P. Short, Breaking the power law: Multiscale simulations of self-ion irradiated tungsten, *Journal of Nuclear Materials* **504**, 33 (2018).
- [71] J.-H. Ke and A. M. Jokisaari, Effects of aluminum and molybdenum on the phase stability of iron-chromium alloys: A first-principles study, *JOM* **75**, 3208 (2023).